Journal of Materials Chemistry A

ROYAL SOCIETY OF CHEMISTRY

PAPER

View Article Online
View Journal | View Issue

Cite this: J. Mater. Chem. A, 2022, 10, 10593

Applications of advanced metrology for understanding the effects of drying temperature in the lithium-ion battery electrode manufacturing process†

Ye Shui Zhang, *[abc] Josh J. Bailey, [abd] Yige Sun, [be] Adam M. Boyce,[ab] Will Dawson, [ab] Carl D. Reynolds, [bf] Zhenyu Zhang,[ab] Xuekun Lu, [ab] Patrick Grant,[be] Emma Kendrick, [bf] Paul R. Shearing [ab] and Dan J. L. Brett *[ab]

The performance of lithium-ion batteries is determined by the architecture and properties of electrodes formed during manufacturing, particularly in the drying process when solvent is removed and the electrode structure is formed. Temperature is one of the most dominant parameters that influences the process, and therefore a comparison of temperature effects on both NMC622-based cathodes (PVDF-based binder) and graphite-based anodes (water-based binder) dried at RT, 60, 80, 100 and 120 °C has been undertaken. X-ray computed tomography showed that NMC622 particles concentrated at the surface of the cathode coating except when dried at 60 °C. However, anodes showed similar graphite distributions at all temperatures. The discharge capacities for the cathodes dried at 60, 80, 100 and 120 °C displayed the following trend: 60 °C < 80 °C < 100 °C < 120 °C as C-rate was increased which was consistent with the trends found in adhesion testing between 60 and 120 °C. Focused-ion beam scanning electrode microscopy and energy-dispersive X-ray spectroscopy suggested that the F-rich binder distribution was largely insensitive to temperature for cathodes. In contrast, conductivity enhancing fine carbon agglomerated on the upper surface of the active NMC particles in the cathode as temperature increased. The cathode dried at RT had the highest adhesion force of 0.015 N mm^{-1} and the best electrochemical rate performance. Conversely, drying temperature had no significant effect on the electrochemical performance of the anode, which was consistent with only a relatively small change in the adhesion, related to the use of lower adhesion water-based binders.

Received 31st January 2022
Accepted 11th April 2022

DOI: 10.1039/d2ta00861k

rsc.li/materials-a

1. Introduction

Lithium-ion batteries (LIBs) have been widely applied in portable electronic devices and state-of-the-art electric vehicles due to their high energy and power density.[1] To maintain consistency within cell electrodes, a homogeneous and defect-free electrode coating is required to enable uniform current densities and to facilitate lithium-ion transport between electrodes, reducing degradation and failures rates.[2] The porous electrode structure, and physical, mechanical and electrochemical properties of the electrode coatings are extremely important in maintaining good consistency in LIBs. The electrode physico-chemical properties are controlled by the mixing, coating and, most importantly, the drying and subsequent calendering processes, which in turn relate to the various parameters/variables during the drying process (DP).[3–5] The three-stage drying mechanism is illustrated in Fig. 1.

Temperature is known to play an important role in the DP as a key parameter that influences drying rate. For example, high temperatures lead to binder migration (typically to the upper free surface), reducing the adhesive strength between the coating layer and the current collector (CC). This can result in the delamination of the coating from the CC, electrode shrinkage and coating component segregation;[7–10] which in turn increases the internal resistance of the electrode through poor adhesion and cohesion properties[7,11] and decreases cell capacity.[12]

[a]Electrochemical Innovation Lab, Department of Chemical Engineering, University College London, London, WC1E 7JE, UK. E-mail: d.brett@ucl.ac.uk; yeshui.zhang@ucl.ac.uk

[b]The Faraday Institution, Quad One, Harwell Science and Innovation Campus, Didcot, OX11 0RA, UK

[c]School of Engineering, University of Aberdeen, Aberdeen, AB24 3UE, UK

[d]School of Mechanical and Aerospace Engineering, Queen's University Belfast, Belfast, BT9 5AH, UK

[e]Department of Materials, University of Oxford, Parks Road, Oxford, OX1 3PH, UK

[f]School of Metallurgy and Materials, University of Birmingham, Birmingham, B15 2TT, UK

† Electronic supplementary information (ESI) available: Supporting data for adhesion force tests and electrochemical testing results. See https://doi.org/10.1039/d2ta00861k

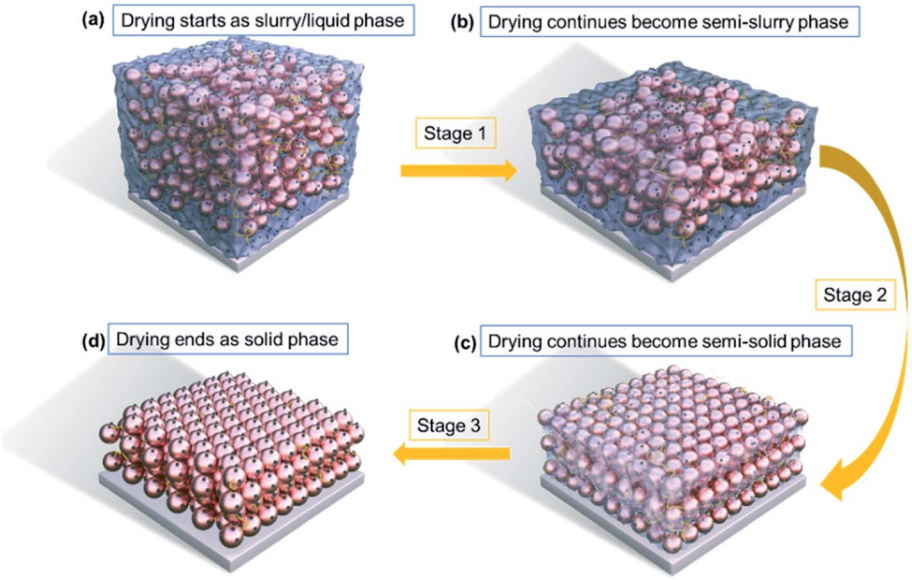

Fig. 1 The three-stage drying mechanism. (a) Stage 1 is from slurry phase to form a semi-slurry, (b) Stage 2 follows, with further removal of solvent and (c) Stage 2 ends with a compacted solid coating, shown in (d). (Yellow strings indicate the binder, pink particles indicate active material particles, black dots indicate the conductive carbon and light blue colour indicates the solvent.) Adapted with permission from ref. 6. Copyright {2021} American Chemical Society.

Recent modelling work by Lombardo *et al.*[13] applied a physics-based three-dimensional model to mimic additive migration during drying; this simulated the effect of drying rate on the final electrode mesostructure and the dynamics of additive migration. Tsotsas and Mujumdar[14] described different types of modelling: continuum-level models based on volume-averaging, pore-network models, continuous thermomechanical models and computational fluid dynamics. Defraeye *et al.*[15] considered convective heat and mass transfer modelling at air-porous material interfaces. Iqbal *et al.*[16] used a coupled electrochemical–mechanical and cohesive-zone finite-element model to study mechanical failure at the interface between graphite particles and polyvinylidene fluoride (PVDF) binder in LIBs. Tirumkudulu *et al.*[17] and Yow *et al.*[18,19] studied the critical stress of cracking in drying latex films.

Although modelling studies have led to new insights into electrode DP, experimental investigations are required for definitive analysis and to validate such models. Zhang *et al.*[2] recently reviewed the most up-to-date metrologies which have been applied, or have the potential to be applied, to study the DP of LIBs. For example, scanning electron microscopy (SEM) with energy-dispersive X-ray spectroscopy (SEM-EDS) has become a powerful technique to investigate the binder migration behaviour of LIB electrodes occurring during the DP. Jaiser *et al.*[20] not only investigated microstructure formation in LIB electrodes during drying, but also component gradients for anode coating cross-sections at different stages of drying using EDS under cryogenic conditions. The liquid phase binder and solvent diffusion were both implicated in the binder gradients of dried electrodes by "dragging" the binder to the surface with capillary forces.[20] Westphal *et al.*[3] used SEM-EDS to detect fluorine concentration to indicate binder distribution inside an electrode coating. EDS was used to map the fluorine distribution through the electrode coating layer, showing that the binder was more concentrated at the top layer of the electrode coating. The binder distribution was also investigated within an electrode made with water-based binders, such as styrene butadiene rubber (SBR) and carboxymethyl cellulose (CMC). Sodium is the typical element in CMC which is used to map these binder distributions by EDS.[21,22]

To investigate the porosity and pore size distribution (PSD) of the electrode microstructures futher, multi-scale X-ray computed tomography (CT) has been applied to characterize the electrodes.[23–28] Westhoff *et al.* created a framework for stochastic 3D modelling of the microstructure of electrodes and the structures were validated by 3D tomography.[23] Danner *et al.*[24] employed synchrotron X-ray tomography to create 3D microstructure models of electrodes for battery performance. Ebner *et al.*[28] used synchrotron X-ray tomographic microscopy to statistically characterize the microstructure of transition metal oxide-based electrodes. The authors introduced their segmentation algorithm to be able to identify each of the particles and evaluate the PSD; the calculated PSD was consistent with the PSD obtained by experimental work by laser diffraction. Rahe *et al.*[26] used nanoscale X-ray CT to investigate the structural change in aged automotive LIB cells; the CT images showed the morphology of the electrodes in terms of their internal porous structure. The porosity of aged anodes was reduced due to organic residues and depositions that were quantified and visualized by CT imaging and analysis. Mapping the 3D microstructure of electrodes, rather than 2D cross-sections only, is recognized as increasingly important for understanding any structural heterogeneity and its corresponding effects on battery performance. X-ray CT has also been

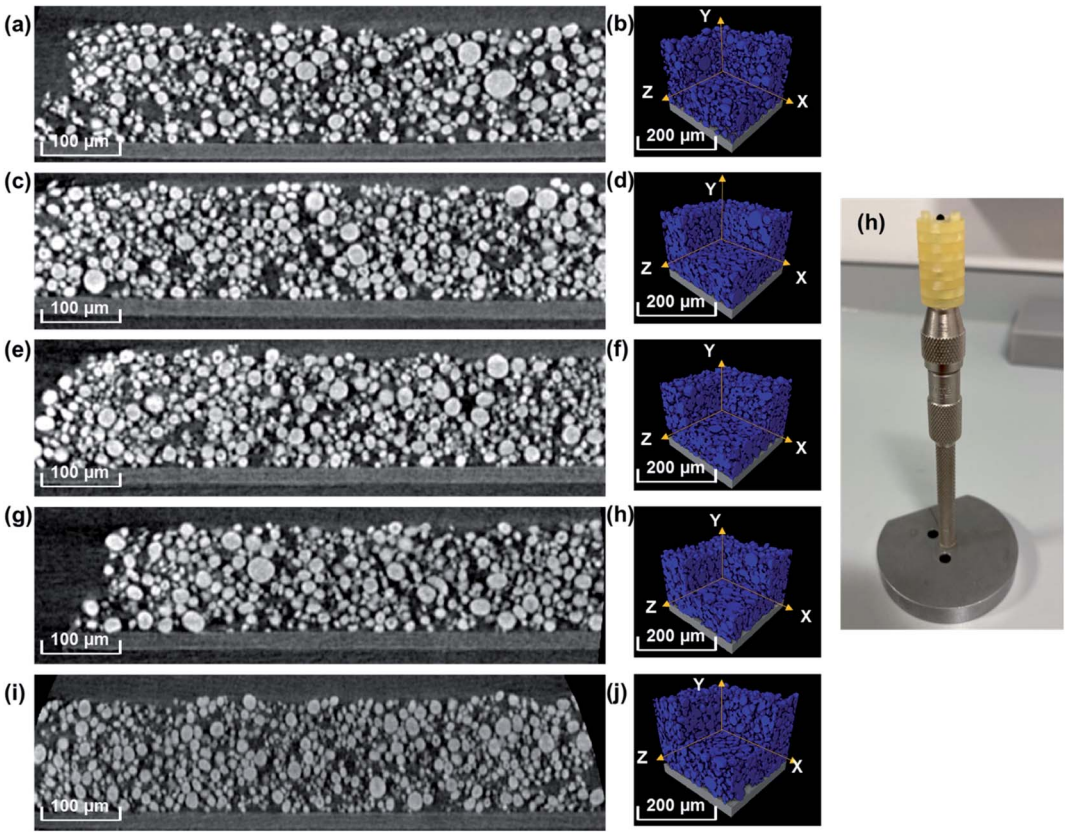

Fig. 2 XZ-slices from tomograms of cathode coatings dried at (a) RT, (c) 60 °C, (e) 80 °C, (g) 100 °C, and (i) 120 °C; segmented AM particles of cathode coatings dried at (b) RT, (d) 60 °C, (f) 80 °C, (h) 100 °C and (j) 120 °C; (h) bespoke 3D printed holder for rapid, multiple-recipe X-ray micro-CT imaging.

applied *in situ* to determine microstructure evolution during battery degradation.[4,29–31]

Overall, the drying of wet electrode films is complex and known to critically influence final physico-chemical performance, but the drying dynamics are poorly understood. To better manipulate electrode structure and properties in the DP, it is useful to correlate and/or integrate multiple drying analysis methodologies to understand better the effect of each parameter. In this paper we undertake a comprehensive study of the effect of temperature on the drying of LIB electrodes (both NMC622-based cathodes with PVDF-based binder and graphite-based anodes with water-based binder, which are both commonly used in LIBs). The investigation involves several advanced characterization methods, including X-ray CT for analysing electrode active material (AM) distributions; adhesion testing of the electrode coating on CC using the axial capability of a rheometer; a focused-ion beam/scanning electrode microscopy with energy-dispersive X-ray spectroscopy (FIB-SEM-EDS) to study binder distribution in electrodes; and electrochemical analysis of electrodes dried at different temperatures. The findings provide a deeper understanding of the temperature effects during the DP of LIB electrodes, which will hopefully benefit and shorten process optimization for LIB manufacturing.

2. Materials and experimental set-up

2.1 Materials

The recipes for both cathodes and anodes in this work are industrially relevant formulations.[32] The cathode slurry consisted of 96 wt% $LiNi_{0.6}Mn_{0.2}Co_{0.2}O_2$ (NMC622, BASF), 2 wt% PVDF (Solvay) and 2 wt% C_{65} (Imerys). The anode slurry consisted of 95.25 wt% artificial graphite (S360 E3 Artificial Graphite, BTR), 1.5 wt% CMC (BVH8, Ashland), 2.25 wt% SBR (BM451-B, Zeon), and 1 wt% C_{45} (Imerys). All powders were dried at 120 °C in a vacuum oven over 12 h to remove moisture. Details of the procedure for making the electrode slurries and coatings have been reported previously.[32] A THINKY mixer (ARE-20, Intertronics) was used to mix the cathode binder solution (PVDF and *N*-methyl pyrrolidone, NMP) at 2000 rpm for 15 min until the solution became homogenous. Then, NMC622 and C_{65} were added slowly to the binder solution to form a slurry with a solid content ~60 wt%. The slurry was then mixed again at 2000 rpm for two periods of 15 min, 5 min apart, to cool down the slurry. The homogenous slurry was degassed in the THINKY mixer at a speed of 2000 rpm for 2 min. To prepare the anode slurry, CMC was firstly pre-dissolved in water to make a 1.5% solution. The weighed graphite, C_{45}, the 1.5% CMC solution and SBR were added into a THINKY pot to form a slurry with 44 wt% solid content. The mixing procedure was

the same as that used for the cathode slurry preparation. The cathode slurry was then coated onto a piece of aluminium foil with thickness ~16 μm (PI-KEM) using a doctor blade thin-film applicator (calibrated with a metal shim), resulting in a wet electrode of ~280 μm thickness. The anode slurry was coated on a copper foil with thickness ~9 μm (Phi-Chem) using a similar procedure, resulting in ~300 μm thick slurry coating. The slurry cast coatings were subsequently dried on a pre-heated hotplate (Nickel-Electro Clifton HP1-2D) with digital control and an aluminium plate (457w × 305d mm) at room temperature (RT), 60, 80, 100 and 120 °C. The drying process was conducted inside of a fumehood with temperature and moisture control.

2.2 X-ray computed tomography

An A Series/Compact Laser Micromachining System (Oxford Lasers, Oxford, UK) with an embedded Class 4, 532 nm wavelength laser was used to prepare samples for X-ray CT characterization. All cathodes were cut into 2 mm discs and anodes were cut into 500 μm discs. All X-ray CT imaging was performed using a Zeiss Xradia 520 Versa (Carl Zeiss Microscopy Inc., Pleasanton, US) micro-CT instrument. X-ray CT scans were carried out with an X-ray source tube voltage of 60 kV with an exposure time of 15 s per projection image for cathodes and 60 s for anodes. A total of 901 projection images were collected per scan with a 20× lens for cathodes and 1201 projections were collected for anodes. Reconstruction of the radiographic data was achieved using a cone-beam filtered back-projection algorithm implemented in Zeiss Scout and Scan software resulting in a reconstructed voxel size of ~0.33 μm. Post-processing of the reconstructed CT data was conducted using Avizo 9.4 (Thermo Fisher Scientific, UK) and ilastik (machine-learning-based, open-source segmentation software[33]) for evaluation of AM particle distributions.

2.3 Adhesion testing

Adhesion testing was performed using a Netzsch Kinexus Pro+ Rheometer following a 180-degree peel method devised in-house. A 25 mm-wide piece of double-sided tape was attached to a section of coating, and the free end of the coating and the tape attached to the upper and lower rheometer geometry, respectively. These were driven apart at 10 mm s^{-1} to enact a 180-degree peel (fully removing the coating from the substrate) with axial force measurement from the rheometer. The force was recorded in a region where the axial force measurement was stable and peeling was visually consistent.[34] This was repeated on six samples for each coating to take an average and normalized by the width of the tape to give the force per unit length required to peel the coating from the substrate.

2.4 Focused-ion beam/scanning electrode microscopy with energy-dispersive X-ray spectroscopy

The equipment used for microscopic observation, cross-sectioning, and elemental mapping was a Thermo Scientific™ Helios™ G4 PFIB CXe DualBeam™ FIB/SEM combined with EDS (Oxford EDS, Ultim max 170 SDD detector). The electrodes were dried at various temperatures and then glued onto sample holders with Acheson silver dag (Agar Scientific, UK). A 5 μm-thick Pt layer was deposited on the area of interest. The primary beam was a Xe^+ plasma source at 30 keV, incident on the surface of the electrode and operated with a range of currents from 15 nA to 0.2 μA for sectioning and milling with reduced beam damage. For elemental mapping of the fabricated cross-sections, EDS was used. An electron beam was perpendicular to the cross-section for imaging and for exciting the characteristic X-rays of the elements in the area of interest. All the secondary electron images and EDS maps were collected at 10 kV, 1.6 nA. Aztec software (Oxford Instruments, AZtec 4.1 SP1) was used to analyze the mapping results.

2.5 Electrochemical performance test

The electrodes were cut into 15 mm discs for coin cells. A Celgard separator was cut into 19 mm discs to avoid short circuits. All the coin cell components, namely the cut electrodes, separators, and other coin cell parts (spacer thickness was 1 mm) were dried overnight in a vacuum oven at 80 °C to remove any moisture before assembly. 70 μL of electrolyte (Solvionic, 1 mol L^{-1} lithium hexafluorophosphate in (1 : 1 vol%) ethylene carbonate : dimethyl carbonate with 2 wt% vinylene carbonate – 99.9%) was filled in each of cell. After the assembly of the coin cells, a formation step composed of two CC–CV charge–discharge cycles at a C-rate of C/20 (C/50 cut-off) was conducted within a voltage window of 2.5 to 4.2 V *vs.* Li/Li^+ for cathode half-cells and 0 to 2.5 V *vs.* Li/Li^+ for anode half-cells, where the half cells contained a lithium metal counter electrode. Electrochemical testing was carried out using a BCS-805 Biologic battery cycler (Biologic, France). The cells were then charged at a constant current C/10 and corresponding to discharged C-rates of C/10, C/5, C/3, C, 2C and 3C.

3. Results and discussion

3.1 Effects of drying temperature on active material particle distribution within electrodes

Reconstructed 2D orthoslices and 3D volume renderings of the cathodes dried at RT, 60, 80, 100 and 120 °C are shown in Fig. 2. The NMC622 particles are clearly visible in Fig. 2(a), (c), (e), (g) and (i), where NMC 622 particles appear as round, light grey shapes, and the pores and binder occupy the gaps between particles. A cubic volume rendering, with 200 μm dimensions, of the segmented AM particles for each cathode sample is shown in Fig. 2(b), (d), (f), and (h), illustrating the internal structure of the cathode coatings. Fig. 2(h) is a bespoke 3D printed holder for rapid, multiple-recipe X-ray micro-CT imaging with Versa CT as used in a previous study.[35] The X-ray attenuation coefficient is much greater for the NMC622 particles than either the pore or the carbon binder domain (CBD) and thus the particles can be clearly identified according to their higher grayscale values, allowing for ready segmentation and further AM distribution analysis. It should be noted that it has been reported that the application of X-ray CT for characterizing LIB electrodes (at this length scale) comes with limitations for identifying the CBD, in which the pore and CBD

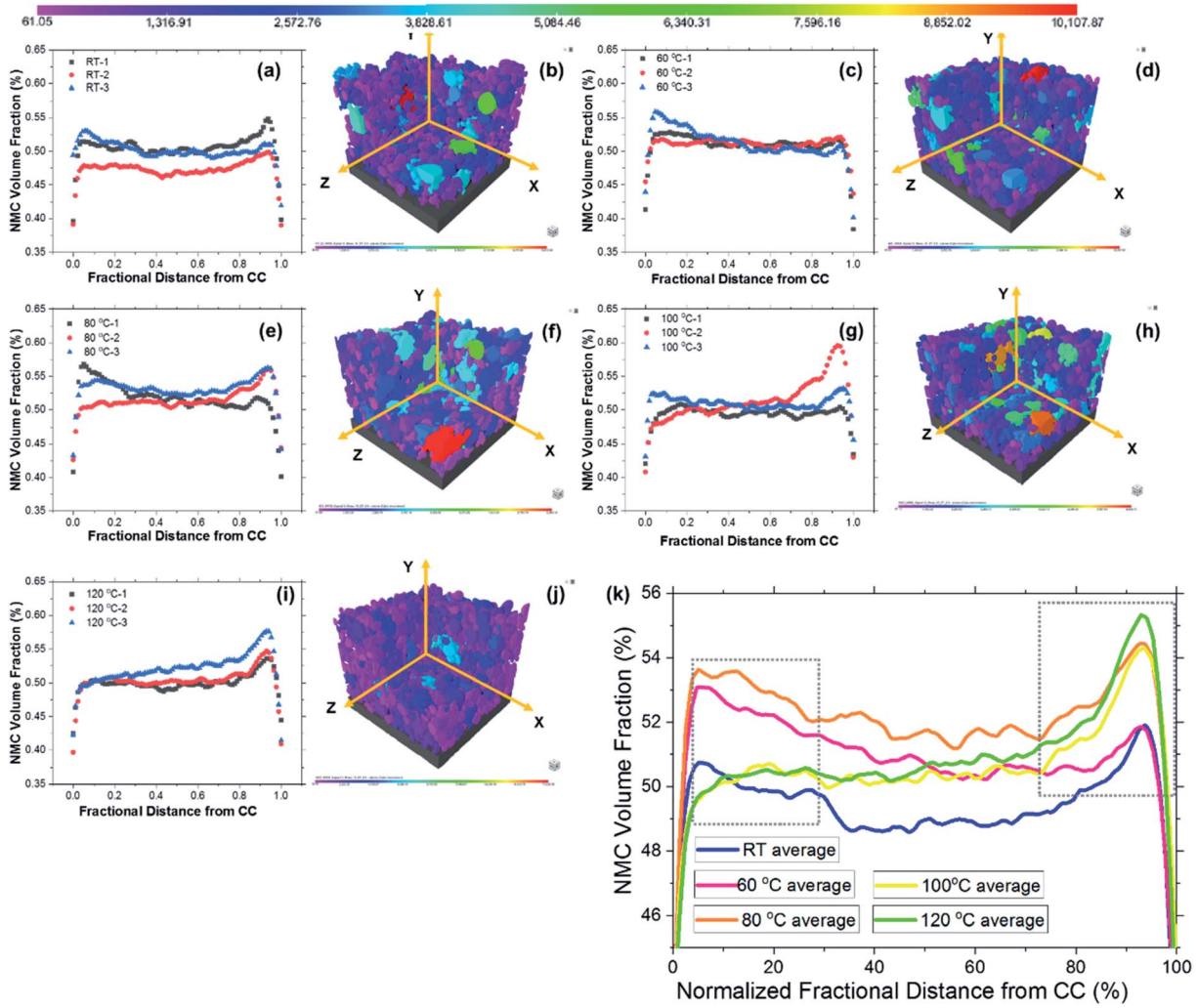

Fig. 3 Areal fraction plots as a function of distance from the CC, illustrating through-plane inhomogeneity for cathodes dried at different temperatures: (a) RT, (c) 60 °C, (e) 80 °C, (j) 100 °C and (i) 120 °C; corresponding volume renderings of the electrode active particles dried at (b) RT, (d) 60 °C, (f) 80 °C, (h) 100 °C and (i) 120 °C, where the colour scale bar indicates the different size of the AM particles; (k) average areal fraction of AM as a function of distance from the CC for cathodes dried at different drying temperatures (error bar is in Fig. S1†).

of the electrode are observed as a single phase.[36,37] Therefore, this work uses X-ray CT as a powerful tool to analyse only the AM distribution through the coating layer.

Areal fraction plots as a function of distance from the CC to the surface of the coating illustrating through-plane inhomogeneity for cathodes dried at different temperatures are shown in Fig. 3(a), (c), (e), (g) and (i). Each electrode was scanned three times for three different samples to improve the statistical robustness of the results, displaying similar AM distributions across the repeated scans. Corresponding volume renderings of the segmented electrode active particles dried at different temperatures are shown in Fig. 3(b), (d), (f), (h) and (j). The different colours of the round particles indicate the size of the particles. The particle size distribution is dominated by the NMC622 particles which will not be affected by the drying process. The average areal fractions of AM as a function of distance from the CC for cathodes dried at different temperatures are also plotted, as shown in Fig. 3(k). In Fig. 3(a), (c), (e), (g) and (i), the results show the different behavior of AM distributions for cathodes dried at different temperatures. For all samples except 60 °C, more NMC622 particles accumulated at the coating surface, as shown in Fig. 3(a), (e), (g) and (i). However, in Fig. 3(a), (c) and (e), there is an accumulation of NMC622 particle fractions near the CC for cathodes dried at RT, 60 and 80 °C. Conversely, in Fig. 3(g) and (i), there is a relatively even NMC622 particle distribution near the CC for cathode dried at 100 and 120 °C.

Reconstructed 2D orthoslices and 3D volume renderings of the anodes dried at RT, 60, 80, 100 and 120 °C are shown in Fig. 4(a), (c), (e), (g) and (i). The graphite particles are clearly visible, where their irregular shape is light grey, and the pores and binder occupy the gaps between graphite particles. Cubic volume renderings of each anode are shown in Fig. 4(b), (d), (f), (h) and (j), illustrating the 3D structure of the anode coatings. As with the cathodes, the graphite particles (AM) were readily

segmented *versus* the background due to higher X-ray attenuation *versus* pore space and CBD.

As with the triplicate results for cathodes shown in Fig. 3, the AM distribution derived from X-ray CT scans of the cathodes showed high repeatability. The areal fraction of anode AM (graphite) as a function of distance from the CC for anodes dried at different temperatures is plotted in Fig. 4(k). The results show similar behavior for graphite distributions for anode dried at RT, 60, 80, 100 and 120 °C, with no significant difference in AM distributions as a function of temperature. The graphite distribution apparently undulates slightly through the coating, which may due to be the irregular shape of the graphite particles. The results correlate with the electrochemical performance of the anode half-cells, as shown in Fig. 8, with no significant change in capacity. This finding is supported by Li and Wang[38] who investigated binder concentration distributions in dried water-based and organic-based (PVDF-based) binder $LiCoO_2$ electrode sheets and the physical, electrical and electrochemical properties of the electrodes. They showed the organic-based binder electrode had a non-uniform distribution of the electrode components, with greater heterogeneity than water-based binder electrode, which may arise because the 'time-for-segregation' for the anode is shorter than cathode drying.[38] The anodes in this work were prepared with a water-based binder and the cathode was prepared with organic-based binder using NMP as the solvent. NMP has a much

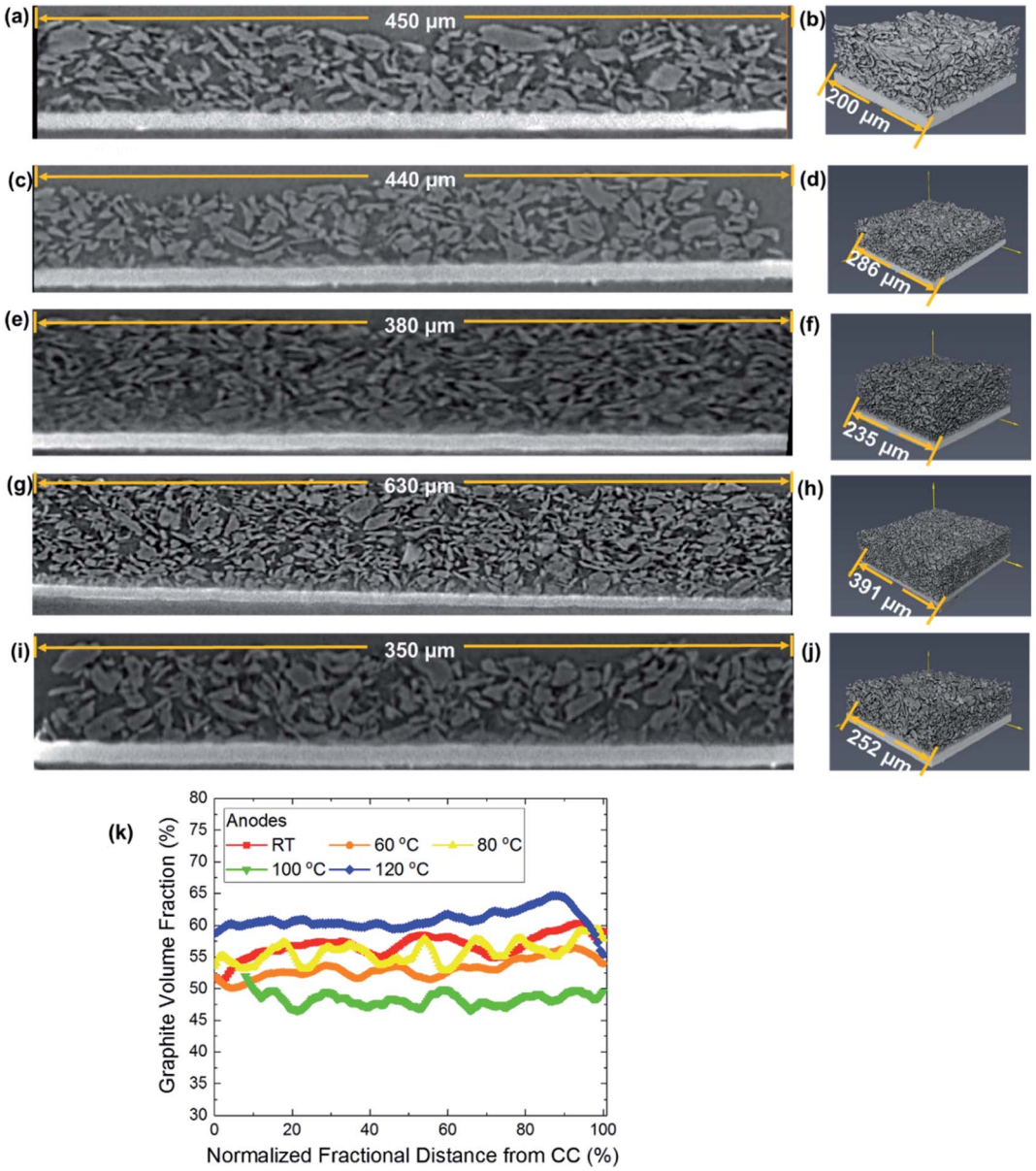

Fig. 4 XZ-slices from tomograms of anode coatings dried at (a) RT, (c) 60 °C, (e) 80 °C, (g) 100 °C and (i) 120 °C; segmented AM particles of cathode coatings dried at (b) RT, (d) 60 °C, (f) 80 °C, (h) 100 °C and (j) 120 °C; (k) areal fraction of graphite as a function of distance from the CC for anodes dried at different drying temperature.

higher boiling point (202 °C) than water such that it takes a longer time to be fully removed by evaporation. Consequently, the reduced drying time for anodes leads to a reduced time-for-segregation, thus providing an even distribution of graphite at all investigated temperatures.

3.2 Effects of drying temperature on adhesion force and binder distribution of the electrode

Adhesion testing for both cathodes and anodes dried at RT, 60, 80, 100 and 120 °C was performed using a Netzsch Kinexus Pro+ rheometer following a 180-degree peel method devised in-house. The electrode dried at each temperature was tested six times to probe the repeatability of the experiments. Adhesion forces for each sample, average adhesion force for each electrode, standard deviation of adhesion force for each electrode, average adhesion force per millimeter and standard deviation of adhesion force per millimeter are shown in Table S1 in the ESI.† A plot of the average adhesion force per millimeter for cathodes dried at different temperatures is shown in Fig. 5(a), and for anodes in Fig. 5(b). For cathodes, there is no significant difference in the adhesion force for those dried from 60 to 120 °C, which is further supported by fluorine mapping by FIB-SEM-EDS in Fig. 6(k)–(o). FIB-SEM micrographs of cathodes dried at RT, 60, 80, 100 and 120 °C are presented in Fig. 6 (a) RT, (b) 60, (c) 80, (d) 100 and (e) 120 °C, respectively. The EDS mapping of fluorine distributions from CC toward the surface of coatings for cathodes dried at different temperatures are shown in Fig. 6 (k) RT, (l) 60, (m) 80, (n) 100 and (o) 120 °C, respectively. The results show no significant differences in fluorine distribution for cathodes dried at different temperatures, implying that all cathodes have a near-homogeneous distribution of binder. Although there is no obvious difference in fluorine distribution, the EDS mapping of carbon distributions for cathodes dried at different temperatures was performed in a different way. These maps are shown in Fig. 6 (f) RT, (g) 60, (h) 80, (i) 100 and (j) 120 °C, which show there is a qualitative impression that the carbon (yellow squares) accumulates more towards the top of the NMC622 particles as the temperature increases, correspondingly there is a tendency for less carbon on the underside of the NMC622 particles (blue squares), although further investigation and a more quantitative approach is required to confirm this impression. Westphal *et al.*,[7] who also investigated the influence of temperature on electrode component segregation, similarly found higher drying temperatures led to greater segregation of inactive materials. Recalling that RT gave the highest adhesion force per millimetre in cathodes, as shown in Fig. 5(a), these effects combine such that in the C-rate discharge capacity tests (Fig. 7), the cathode dried at RT has the highest specific capacity.

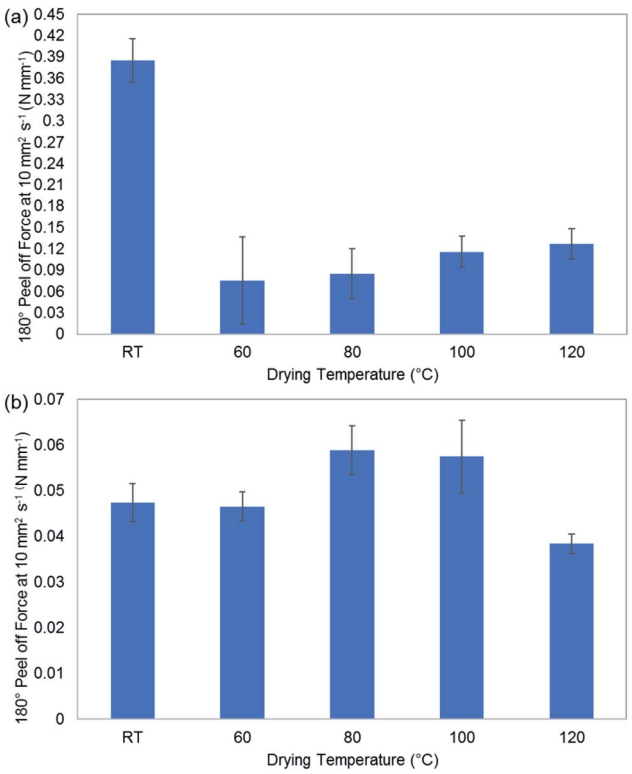

Fig. 5 Average adhesion force for 180°-peel-off at 10 mm s^{-1} for six replicates of each electrode dried at RT, 60, 80, 100 and 120 °C with error bars (standard deviation): (a) cathodes and (b) anodes.

The anodes dried at 80 and 100 °C gave only slightly higher adhesion force per millimeter compared with anodes dried at other temperatures. This is again consistent with Westphal *et al.*,[3] who reported that adhesion strength is independent of mass loading at a relatively low temperature (~80 °C) as the driving force for solvent evaporation is small. However, high temperatures have been reported to potentially lead to greater binder migration (as seen for the NMC cathodes earlier), which can cause anode delamination and result in high resistance.[7–10] Electrode adhesion is strongly dependent upon the drying temperature and higher temperatures result in lower adhesion strength between the copper CC and the coating layer.[7,8,39] However, the thickness of the coatings also needs to be considered, and in the case of graphite,[13] the adhesion strength can also decrease as the drying temperature increases from 80 to 110 °C with mass loadings up to 8.1 g cm^{-2}. In these cases, the temperature played a minor role in electrode adhesion, which was more sensitive to thickness and mass loading. The adhesion results are consistent with the EDS mapping of elemental sodium across the electrode cross-sections, as shown in Fig. 6(u)–(y), which are proxy elements for the binder. Sodium is distributed comparatively evenly across the anodes, regardless of drying temperature. This may be explained by a shorter time-to-fixation, which is indicative of faster polymer entanglement, and subsequently, there is less time for binder segregation. It cannot be ignored that the binder concentration in anodes is very low which leads to less concentrated sodium maps, possibly requiring further investigation. Although higher temperatures will cause faster convection currents towards the surface as solvent is removed, the polymer matrix will also become more rapidly entangled as solvent is lost, resisting this motion, and the two competing effects approximately cancel.

Comparing the adhesion forces for both cathodes and anodes, it is obvious that the adhesion forces in cathodes are much higher than in anodes; for example, the average adhesion

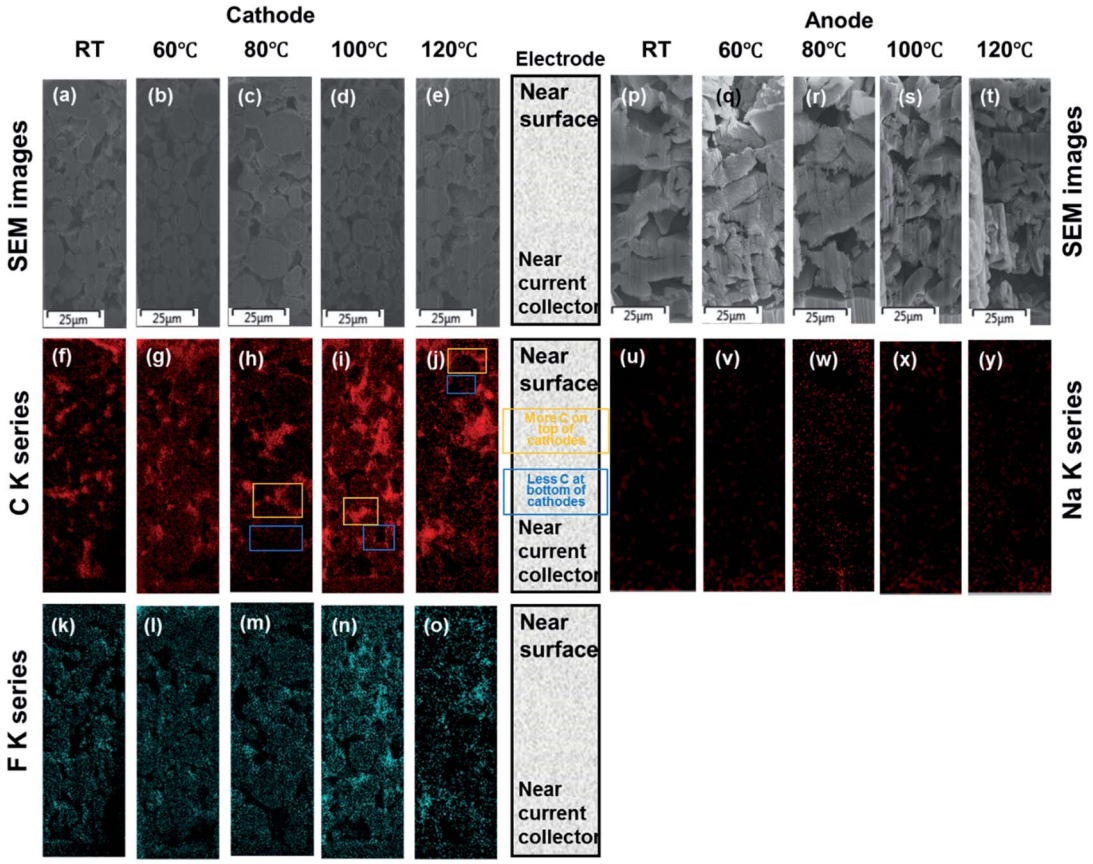

Fig. 6 FIB-SEM micrographs of cathodes dried at (a) RT, (b) 60 °C, (c) 80 °C, (d) 100 °C and (e) 120 °C; EDS mapping of carbon distribution from current collector towards the surface of coatings for cathodes dried at (f) RT, (g) 60 °C, (h) 80 °C, (i) 100 °C and (j) 120 °C; EDS mapping of fluorine distributions for cathodes dried at (k) RT, (l) 60, (m) 80, (n) 100 and (o) 120 °C. (Yellow squares highlight the carbon accumulating on the top of the NMC622 particles, blue squares highlight less carbon at the bottom of NMC622 particles.) FIB-SEM micrographs of anodes dried at (p) RT, (q) 60 °C, (r) 80 °C, (s) 100 °C and (t) 120 °C; EDS mapping of sodium distribution from current collector towards the surface of coating for cathodes dried at (u) RT, (v) 60 °C, (w) 80 °C, (x) 100 °C and (y) 120 °C.

forces per millimetre for cathodes and anodes dried at 80 °C are 0.0034 and 0.0024 N mm^{-1}, respectively. This finding is consistent with the literature that states that organic-based binders provide higher adhesion force than water-based binders.[32,38] The inferior wetting of aqueous slurries on the CC leads to higher surface tension and lower adhesion strength, potentially reducing the cycle life of the cell.[40–42] Moreover,

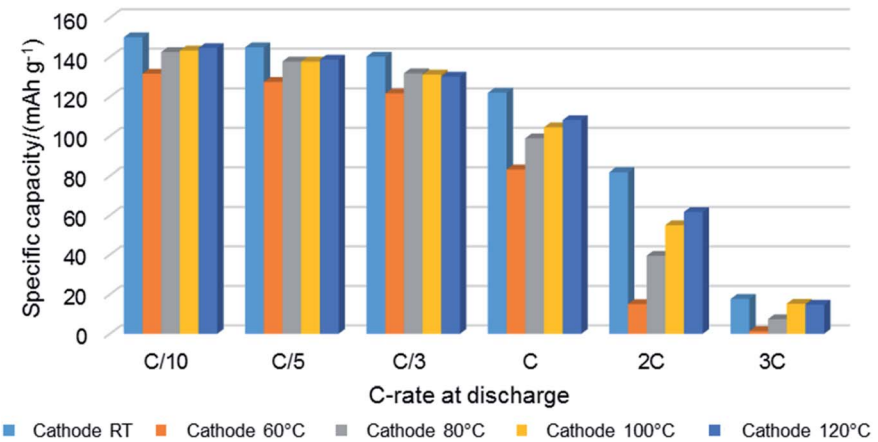

Fig. 7 Specific discharge capacity at different C-rates (C/10, C/5, C/3, C, 2C and 3C) of cathodes dried at different temperatures (RT, 60, 80, 100 and 120 °C).

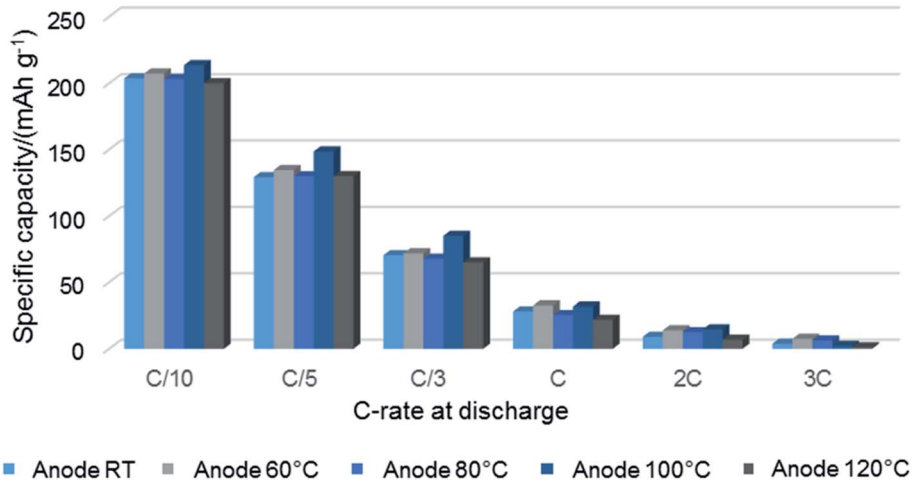

Fig. 8 Specific discharge capacity at different C-rates (C/10, C/5, C/3, C, 2C and 3C) of anodes dried at different temperatures (RT, 60, 80, 100 and 120 °C).

electrodes made from water-based solvents can lead to more cracking without optimum drying protocols.[42–45]

3.3 Effects of drying temperature on the electrochemical performance of electrodes

Electrochemical properties were tested in coin cells with different C-rates of C/10, C/5, C/3, C, 2C and 3C at discharge state, and specific capacity plots for cathodes and anodes are shown in Fig. 7 and 8, respectively. Charge and discharge parameters are shown in Tables S3 and S4 in the ESI.† As expected, the specific capacity of the electrodes (cathodes and anodes) is highest at the lowest C-rate of C/10 for both cathodes and anodes, regardless of drying temperature. Comparing the specific capacity for electrodes dried at different temperatures, the cathodes dried at RT have the highest specific capacity at all C-rates. Conversely, drying temperature does not play a dominant role in dictating the electrochemical performance of the anodes.

In Fig. 7, and Table S3 in ESI,† the discharge performance of the cathode dried at RT has the highest specific capacity of 150.06 mA h g^{-1} at C/10. There are similar findings at other C-rates: cathodes dried at RT have the highest specific discharge capacities at all C-rates, compared with cathodes dried at 60, 80, 100 and 120 °C. The relatively slow drying rate at RT tends to promote a more homogeneous CBD distribution, which will enhance the electrochemical performance of the electrode. The assumption is supported by the EDS mapping of carbon and fluorine, as shown in Fig. 6 (f, k) RT, (g, l) 60, (h, m) 80, (i, n) 100 and (j, o) 120 °C, where the fluorine distribution is not significantly affected by drying temperature. While carbon tends to accumulate more on the top of the AM particles as the temperature increases (yellow circles), this segregation is more localised in length-scale, and needs firmer quantification. While there was no significant difference in cathode binder distribution according to EDS at the different temperatures, as shown in Fig. 6(k)–(o), adhesion is affected: the cathode dried at RT has the highest capacity and the highest adhesion of 0.015 N mm^{-1}. The increased adhesion is beneficial both when assembling the cells (less likely to crack/delaminate and incur failure), and also less likely to delaminate during cycling causing poor cycle life.

As shown in Fig. 7, cathodes dried at RT showed consistently higher discharge capacities as a function of C-rate, and the discharge capacity for the cathode dried at 60, 80, 100 and 120 °C presented a trend of 60 °C < 80 °C < 100 °C < 120 °C as C-rate increases. The results are consistent with the adhesion test results (Fig. 5(a)), in that the adhesion force for cathodes dried at 60, 80, 100 and 120 °C display a similar trend of 60 °C < 80 °C < 100 °C < 120 °C. As shown in Fig. 8, the specific capacity of the anodes dried at different temperatures do not display a clear trend or major difference. The results are consistent with the adhesion force test as shown in Fig. 5(b) that the adhesion forces for anodes dried at different temperatures are similar. The results are also supported by the similar distribution of AM, as plotted in Fig. 4(h), although it may be harder to identify differences in anode adhesion due to the generally much smaller values.

4. Conclusion

Drying temperature effects on LIB electrodes have been investigated using a variety of characterization methods, and the inter-related aspects of active materials distribution, electrode adhesion and carbon-binder distribution elucidated. The electrochemical performance of NMC622-based cathodes and graphite-based anodes dried at different temperatures ranging from RT to 120 °C has also been studied. The findings are given below:

X-ray CT results show diverse behavior of AM distributions for cathodes dried at different temperatures, with active NMC622 particles tending to concentrate more at the free surface of the electrode coating as drying temperature increases. Meanwhile, NMC622 particles also concentrated near the current collector when dried at relatively low temperatures

of RT, 60 or 80 °C. Conversely, there is an even NMC622 particle distribution near the CC for cathode dried at 100 and 120 °C. This correlates well with the electrochemical results obtained, in that at low C-rates there is not much difference, but as C-rate increases there is a trend of 60 °C < 80 °C < 100 °C < 120 °C for discharge capacity which is consistent with the trend in adhesion force between 60 to 120 °C.

X-ray CT shows similar graphite distributions for anodes dried at each temperature, with no significant trend apparent in areal fraction as a function of distance from the CC.

Although there was no obvious difference in binder distribution obtained by FIB-SEM-EDS fluorine mapping, the EDS mapping of carbon distributions for cathodes dried at different temperatures were performed in a different way showing that carbon accumulated more on the top of the AM particles as the temperature increased.

This work also showed that cathodes dried at RT had the highest adhesion force of 0.015 N mm^{-1}, and that the specific capacity for these cathodes were higher than those dried at higher temperatures for all C-rates.

Comparing the specific capacity for the electrode (cathode and anodes) at different C-rates, the results show that the specific discharge capacity was highest at the lowest C-rate of C/10 for both cathodes and anodes, regardless of the drying temperature.

Comparing the specific capacity for the electrode (cathodes and anodes) dried at different temperatures, the cathode dried at RT had the highest specific capacity at all C-rates.

Conversely, the anode drying temperature did not play a dominant role in determining the electrochemical performance of the anodes, such that the specific capacity of the anodes dried at different temperatures presented no clear trend. These results corresponded well with the adhesion force testing and the distribution of graphite particles.

Author contributions

Conceptualization, Y. S. Z. and D. J. L. B.; methodology, Y. S. Z., J. J. B., Y. S., X. L., Z. Z. and C. D. R.; software, J. J. B., A. B., W. D., X. L., Z. Z. and Y. S. Z.; validation, Y. S. Z., D. J. L. B, P. R. S. and E. K.; formal analysis, Y. S. Z., Y. S., J. J. B., A. B., C. D. R. and W. D.; investigation, Y. S. Z.; data curation, Y. S. Z., Y. S., J. J. B., A. B. and W. D.; writing-original draft preparation, Y. S. Z.; visualization, Y. S. Z., J. J. B., A. B., W. D., X. L., Z. Z. and Y. S.; supervision, D. J. L. B, P. R. S. and E. K.; funding acquisition, D. J. L. B, P. R. S., P. S. G. and E. K.; all authors have read and agreed to the published version of the manuscript.

Conflicts of interest

There are no conflicts to declare.

Acknowledgements

This work was supported by the Faraday Institution [EP/S003053/1 grant number FIRG015]. PRS would like to acknowledge the Royal Academy of Engineering (CiET1718\59) for financial support.

References

1 GVR, *Lithium-ion Battery Market Size, Share & Trends Analysis Report by Product (LCO, LFP, NCA, LMO, LTO, Lithium Nickel Manganese Cobalt), by Application, by Region, and Segment Forecasts, 2020–2027*, Grand View Research, 2020.
2 Y. S. Zhang, N. E. Courtier, Z. Zhang, K. Liu, J. J. Bailey, A. M. Boyce, G. Richardson, P. R. Shearing, E. Kendrick and D. J. Brett, *Adv. Energy Mater.*, 2021, **12**(2), 2102233.
3 B. G. Westphal and A. Kwade, *J. Energy Storage*, 2018, **18**, 509–517.
4 X. Lu, S. R. Daemi, A. Bertei, M. D. Kok, K. B. O'Regan, L. Rasha, J. Park, G. Hinds, E. Kendrick and D. J. Brett, *Joule*, 2020, **4**, 2746–2768.
5 C. D. Reynolds, P. R. Slater, S. D. Hare, M. J. Simmons and E. Kendrick, *Mater. Des.*, 2021, 109971.
6 Y. S. Zhang, A. N. Pallipurath Radhakrishnan, J. B. Robinson, R. E. Owen, T. G. Tranter, E. Kendrick, P. R. Shearing and D. J. Brett, *ACS Appl. Mater. Interfaces*, 2021, **13**, 36605–36620.
7 B. Westphal, H. Bockholt, T. Günther, W. Haselrieder and A. Kwade, *ECS Trans.*, 2015, **64**, 57–68.
8 M. Baunach, S. Jaiser, S. Schmelzle, H. Nirschl, P. Scharfer and W. Schabel, *Drying Technol.*, 2016, **34**, 462–473.
9 H. Hagiwara, W. J. Suszynski and L. F. Francis, *J. Coat. Technol. Res.*, 2014, **11**, 11–17.
10 M. Müller, L. Pfaffmann, S. Jaiser, M. Baunach, V. Trouillet, F. Scheiba, P. Scharfer, W. Schabel and W. Bauer, *J. Power Sources*, 2017, **340**, 1–5.
11 M. Stein, A. Mistry and P. P. Mukherjee, *J. Electrochem. Soc.*, 2017, **164**, A1616–A1627.
12 S. Jaiser, M. Müller, M. Baunach, W. Bauer, P. Scharfer and W. Schabel, *J. Power Sources*, 2016, **318**, 210–219.
13 T. Lombardo, A. C. Ngandjong, A. Belhcen and A. A. Franco, *Energy Storage Mater.*, 2021.
14 E. Tsotsas and A. S. Mujumdar, *Modern Drying Technology*, Wiley Online Library, 2007.
15 T. Defraeye, B. Blocken, D. Derome, B. Nicolai and J. Carmeliet, *Chem. Eng. Sci.*, 2012, **74**, 49–58.
16 N. Iqbal, Y. Ali and S. Lee, *J. Power Sources*, 2020, **457**, 228019.
17 M. S. Tirumkudulu and W. B. Russel, *Langmuir*, 2005, **21**, 4938–4948.
18 H. N. Yow, M. Goikoetxea, L. Goehring and A. F. Routh, *J. Colloid Interface Sci.*, 2010, **352**, 542–548.
19 H. N. Yow, I. Beristain, M. Goikoetxea, M. J. Barandiaran and A. F. Routh, *Langmuir*, 2010, **26**, 6335–6342.
20 S. Jaiser, J. Kumberg, J. Klaver, J. L. Urai, W. Schabel, J. Schmatz and P. Scharfer, *J. Power Sources*, 2017, **345**, 97–107.
21 N. Yabuuchi, Y. Kinoshita, K. Misaki, T. Matsuyama and S. Komaba, *J. Electrochem. Soc.*, 2015, **162**, A538.
22 W. J. Chang, G. H. Lee, Y. J. Cheon, J. T. Kim, S. I. Lee, J. Kim, M. Kim, W. I. Park and Y. J. Lee, *ACS Appl. Mater. Interfaces*, 2019, **11**, 41330–41337.

23 D. Westhoff, I. Manke and V. Schmidt, *Comput. Mater. Sci.*, 2018, **151**, 53–64.
24 T. Danner, M. Singh, S. Hein, J. Kaiser, H. Hahn and A. Latz, *J. Power Sources*, 2016, **334**, 191–201.
25 D. Zhang, A. Forner-Cuenca, O. O. Taiwo, V. Yufit, F. R. Brushett, N. P. Brandon, S. Gu and Q. Cai, *J. Power Sources*, 2020, **447**, 227249.
26 C. Rahe, S. T. Kelly, M. N. Rad, D. U. Sauer, J. Mayer and E. Figgemeier, *J. Power Sources*, 2019, **433**, 126631.
27 R. F. Ziesche, T. Arlt, D. P. Finegan, T. M. Heenan, A. Tengattini, D. Baum, N. Kardjilov, H. Markötter, I. Manke and W. Kockelmann, *Nat. Commun.*, 2020, **11**, 1–11.
28 M. Ebner, F. Geldmacher, F. Marone, M. Stampanoni and V. Wood, *Adv. Energy Mater.*, 2013, **3**, 845–850.
29 D. P. Finegan, M. Scheel, J. B. Robinson, B. Tjaden, I. Hunt, T. J. Mason, J. Millichamp, M. Di Michiel, G. J. Offer and G. Hinds, *Nat. Commun.*, 2015, **6**, 6924.
30 X. Lu, A. Bertei, D. P. Finegan, C. Tan, S. R. Daemi, J. S. Weaving, K. B. O'Regan, T. M. Heenan, G. Hinds and E. Kendrick, *Nat. Commun.*, 2020, **11**, 1–13.
31 O. O. Taiwo, D. P. Finegan, D. S. Eastwood, J. L. Fife, L. D. Brown, J. A. Darr, P. D. Lee, D. J. Brett and P. R. Shearing, *J. Microsc.*, 2016, **263**, 280–292.
32 Y. S. Zhang, *ACS Appl. Mater. Interfaces*, 2021, **13**, 36605–36620.
33 S. Berg, D. Kutra, T. Kroeger, C. N. Straehle, B. X. Kausler, C. Haubold, M. Schiegg, J. Ales, T. Beier and M. Rudy, *Nat. Methods*, 2019, **16**, 1226–1232.
34 S. X. Drakopoulos, A. Gholamipour-Shirazi, P. MacDonald, R. C. Parini, C. D. Reynolds, D. L. Burnett, B. Pye, K. B. O'Regan, G. Wang and T. M. Whitehead, *Cell Rep. Phys. Sci.*, 2021, **2**, 100683.
35 J. J. Bailey, J. Chen, J. Hack, M. Perez-Page, S. M. Holmes, D. J. Brett and P. R. Shearing, *J. Power Sources*, 2021, **509**, 230347.
36 S. Müller, J. Eller, M. Ebner, C. Burns, J. Dahn and V. Wood, *J. Electrochem. Soc.*, 2018, **165**, A339–A344.
37 R. E. Garcıa, Y.-M. Chiang, W. C. Carter, P. Limthongkul and C. M. Bishop, *J. Electrochem. Soc.*, 2005, **152**, A255–A263.
38 C.-C. Li and Y.-W. Wang, *J. Electrochem. Soc.*, 2011, **158**, A1361–A1370.
39 A. Gören, D. Cíntora-Juárez, P. Martins, S. Ferdov, M. M. Silva, J. L. Tirado, C. M. Costa and S. Lanceros-Méndez, *Energy Technol.*, 2016, **4**, 573–582.
40 J. Li, C. Daniel and D. Wood, *J. Power Sources*, 2011, **196**, 2452–2460.
41 W. B. Hawley and J. Li, *J. Energy Storage*, 2019, **25**, 100862.
42 Z. Du, K. Rollag, J. Li, S. J. An, M. Wood, Y. Sheng, P. Mukherjee, C. Daniel and D. Wood III, *J. Power Sources*, 2017, **354**, 200–206.
43 D. L. Wood, J. D. Quass, J. Li, S. Ahmed, D. Ventola and C. Daniel, *Drying Technol.*, 2018, **36**, 234–244.
44 I. Doberdò, N. Löffler, N. Laszczynski, D. Cericola, N. Penazzi, S. Bodoardo, G.-T. Kim and S. Passerini, *J. Power Sources*, 2014, **248**, 1000–1006.
45 M. Kuenzel, D. Bresser, T. Diemant, D. V. Carvalho, G. T. Kim, R. J. Behm and S. Passerini, *ChemSusChem*, 2018, **11**, 562–573.